AIAA JOURNAL
Vol. 46, No. 9, September 2008

Computations of Insect and Fish Locomotion with Applications to Unconventional Unmanned Vehicles

Ravi Ramamurti* and William Sandberg†
Naval Research Laboratory, Washington, D.C. 20375

DOI: 10.2514/1.32826

Living creatures such as insects, birds, and fish generate lift and thrust most often by executing large-amplitude wing flapping, possibly with substantial shape deformation from root to tip. The flow for these motions is unsteady, and conventional steady-state aerodynamics is unable to correctly compute the time history of their flapping-force generation. Three-dimensional unsteady computations of flapping about the deforming wing or fin surface are necessary to correctly predict the lift and thrust throughout the flapping cycle. It is only by executing such computations for creatures or vehicles with moving and deforming surfaces that we can gain insights into the time-varying pressure distribution on all surfaces and how that results in flapping-force generation. This can be coupled with visualization of the origination and evolution of body, wing, and wake vorticity. Three-dimensional unsteady flow computations of the flapping flights of the fruit fly, a pectoral-fin swimmer (the bird wrasse), and a variety of unmanned air vehicles were carried out in pursuit of this information. The performance of these flapping wings under gust conditions was also investigated. The effect of fin deformation on the force production was studied. Novel biomimetic vehicles, incorporating information gained from these computations, were designed and built and their performance is described.

Introduction

FOR thousands of years, the study of flight was dominated by attempts to unlock the secrets of flapping wings. Nature's abundant success in bird and insect flight was so overwhelming as to divert attention from other methods of heavier-than-air aviation. Human technology, however, was ill-suited to reproducing biomorphic flight, and the infant science of aerodynamics had virtually no understanding of it. In time, the complexities of the flapping wing were sidestepped by the development of conventional fixed-wing flight configurations. Nevertheless, recent interest in micro aerial vehicles (MAVs) with wingspans of less than 150 mm has focused considerable attention on flapping-foil propulsion. In the low-Reynolds-number ($5000 \leq Re \leq 50,000$) regimes accessed by such tiny aircraft, operating at very low speeds ($\sim$10 m/s), flapping wings are generally more dynamically advantageous than fixed-wing configurations, particularly if operating in gusts or needing to avoid obstacles. Experimental and computational studies are also providing insight into the aerodynamics of actual biological flight, as well as suggesting biomimetic flapping-wing configurations that, although they have no direct counterpart in nature, may be suited to MAVs. It is clear that a large number of creatures achieve their desired flight-performance characteristics by using either active or passive (or both) shape modifications. Meanwhile, advances in microelectronics, micro- and nanoelectromechanical systems (MEMS and NEMS), flexible shape-adaptive materials, and energy storage and conversion technology are bringing the design and construction of truly biomimetic aircraft closer to being realized.

Unmanned aerial vehicles (UAVs) play an important role in reconnaissance and war fighting [1–5]. Recently, MAVs [6] have been of significant interest to the war-fighting and the intelligence-collection communities. MAVs have the potential for providing a new technological capability that can be used not only by the military, but also in commercial applications including law enforcement, environmental hazard detection and assessments, and inspection of the interior of large buildings. There is more to designing micro air vehicles than just scaling down the dimensions of UAVs. The aerodynamics of the MAVs in the low-Reynolds-number Re regime differ significantly from the aerodynamics of mini vehicles such as the UAVs. As Shyy et al. [7] pointed out, the decreasing size of MAVs makes them much more vulnerable to the fluctuating magnitude and direction of gusts. This potentially results in uncontrollable forces and moments or, at the very least, demands for power that cannot be met. Shyy et al. [8] computationally investigated the performance and demonstrated the benefits of unsteady flow conditions of flexible profiles enabling camber variation over traditional rigid low-Reynolds-number airfoil profiles. Their ability to adapt to the spanwise variation of the inflow velocity, as is easily observed in the leading edges of bird wings, is of great potential value. We are just at the beginning in our attempts to understand the many roles of living creature's shape modifications in response to their environment. Although it is inspirational and possibly useful to attempt to mimic the flight of birds or insects, it is also possible to use flapping-foil propulsion in ways that are inspired by biological flight but do not copy it directly. We have, as operational requirements drive the size of our designs smaller, been guided by a number of biological investigations into the flapping flight of insects and the flapping-fin swimming (flight) of fish.

Recent research efforts of Dickinson et al. [9], Ellington [10], and others have yielded insights into flapping-wing propulsion that are now beginning to be successfully used in MAV designs. These experimental investigations have provided valuable data on kinematics, forces, and wakes that are necessary for subsequent validation of computational studies. Numerous investigators have carried out 3-D computations of hovering flight. Liu and Kawachi [11] obtained qualitative agreement for the computed 3-D flow patterns over a hovering hawkmoth with the wind-tunnel leading-edge-vortex (LEV) visualizations of Willmott and Ellington [12]. Aono and Liu [13] extended this investigation to higher-Reynolds-number computations to describe how the structure of the LEV and spanwise flow changes over the lower-Reynolds-number hovering case. Their results showed the increasing importance of spanwise flow on the LEV and the decreasing importance of viscosity on force production as the Reynolds number increases from 134 to 6300. Sun and Tang [14] computed the unsteady aerodynamics of the hovering *Drosophila* and obtained behavior similar to the measured data, but

Received 18 June 2007; revision received 9 November 2007; accepted for publication 28 November 2007.

*Aerospace Engineer, Laboratory for Computational Physics and Fluid Dynamics, Code 6410. Associate Fellow AIAA.

†Deputy Director, Laboratory for Computational Physics and Fluid Dynamics, Code 6401.

with lower magnitudes. Sun and Wu [15] continued these computations to analyze force production mechanisms in forward flapping flight, finding that delayed stall is still an operational mechanism for lift production. Ramamurti and Sandberg [16] computed the force production in *Drosophila* and obtained nearly exact agreement with the measured force data of Dickinson et al. [9]. Ramamurti and Sandberg [17] also carried out 3-D unsteady computations of insect maneuvering. The computed force production throughout the saccade maneuver was again in nearly exact agreement with measured forces of Fry et al. [18].

The objective of this paper is to investigate the thrust and lift production in flapping foils that can be directly used for the design of unmanned vehicles. Computations are performed to understand the mechanisms of the lift generation in both the hovering and the maneuvering fruit fly. For vehicles with very small inertia, as in the case of MAVs, changes in wing loading can immediately affect the flight path. The need for suppressing the effects of wind gusts becomes important, more so when the airspeed of the vehicle decreases, because wind gusts become a large percentage of the mean airspeed of the vehicle. This is further complicated by the fact that the gusts are not always head-on. Because control of these vehicles is one of the most important problems, it is important to suppress unwanted and sudden changes in direction, elevation, and orientation. Thus, the performance of these flapping wings under gust conditions is also investigated.

We also investigate the underwater counterpart: unmanned underwater vehicles (UUVs) with the unconventional flapping-fin propulsion. In our case, we decided that development of a flexible vehicle was not as likely as a rigid vehicle and therefore chose to look at swimmers that propelled themselves primarily with fins. Hence, we ruled out undulatory swimmers from the start. We explicitly selected control surfaces as the ultimate design objective, as opposed to the vehicle hull itself. For this purpose, we use the kinematics data of the fin motion obtained by Walker and Westneat [19] for the bird wrasse fish. Ramamurti et al. [20] computed the flow past the swimming bird wrasse and compared it with the acceleration data of Walker and Westneat [19]. We chose to investigate the force production by flapping pectoral fin in the bird wrasse fish, to study the effect of fin deformation on the force production and to incorporate that understanding into the design of unmanned underwater vehicles.

Incompressible Flow Solver

The governing equations employed are the incompressible Navier–Stokes equations in arbitrary Lagrangian–Eulerian formulation, which are written as

$$\frac{\partial \boldsymbol{v}}{\partial t} + \boldsymbol{v}_a \cdot \nabla \boldsymbol{v} + \nabla p = \nabla \cdot \sigma \tag{1}$$

$$\nabla \cdot \boldsymbol{v} = 0 \tag{2}$$

where p denotes the pressure, $\boldsymbol{v}_a = \boldsymbol{v} - \boldsymbol{w}$ is the advective velocity vector (flow velocity $\mathbf{v}$ minus mesh velocity w), and both the pressure p and the stress tensor σ have been normalized by the (constant) density ρ. These equations are discretized in time using an implicit time-stepping procedure. It is important for the flow solver to be able to capture the unsteadiness of a flowfield, if such exists. The present flow solver FEFLO is time-accurate, allowing local time stepping as an option. The resulting expressions are subsequently discretized in space using a Galerkin procedure with linear tetrahedral elements. To be as fast as possible, the overhead in building element matrices, residual vectors, etc., should be kept to a minimum. This requirement is met by employing simple low-order elements that have all the variables (u, v, w, and p) at the same node location. The resulting matrix systems are solved iteratively using a preconditioned gradient algorithm. The details of the flow solver have already been discussed extensively elsewhere (Ramamurti et. al. [21–24]) in connection with successfully validated solutions for numerous 2-D and 3-D, laminar and turbulent, and steady and unsteady flow problems.

Discussion of Results

As part of the Naval Research Laboratory (NRL) MAV program, a number of exploratory miniature flight test vehicles have been designed and built to explore various vehicle design configurations, including a range of propulsion and control approaches. The designs focused on minimum-size air vehicles that were capable of performing potentially useful military missions. These vehicles were hand-launched, dual-propeller-driven fixed-wing vehicles. Several of these micro tactical expendable (MITE) vehicles were developed as a result of this research effort and are described by Kellogg et al. [25]. Computational fluid dynamics (CFD) plays an important role in the design of low-Reynolds-number UAVs or MAVs. The flow solver FEFLO was used to investigate a range of small vehicles suitable for autonomous flight operation. We use CFD for two objectives: One is to determine optimal configurations from the aerodynamic performance point of view. The other is to determine the aerodynamic coefficients that serve as input to our six-degree-of-freedom flight simulator. This simulator is in turn used to evaluate stability, performance, and optimal control laws for the autopilot. The aerodynamic characteristics of the MITE vehicle are detailed in Ramamurti and Sandberg [26].

Flapping Propulsion

Recent interest in MAVs with wingspans of less than 150 mm has focused attention on unconventional methods of flight, including flapping-airfoil propulsion. There are several reasons for this growing interest in the age-old fascination with nature's flight mechanisms. First, in the low-Reynolds-number ($2000 \leq Re \leq 30,000$) and low-speed (2–5 m/s) regimes applicable to very small air vehicles, degradation in airfoil performance caused by viscous boundary-layer effects significantly reduces efficiency of the conventional rigid wing and, in particular, the propeller [27]. These effects include significant increases in profile drag coefficient, reduction in maximum lift coefficient, and often a large hysteresis in the change of lift coefficient with the change and rate of change of the angle of attack. Although the average propeller blade's airspeed is higher than that of the wing airfoil, the propeller blade chord is at least one order of magnitude smaller than the wing chord. Whereas the wing of an MAV may be sized to operate just outside this Reynolds number regime, at least part of the propeller blade will be operating within it. Flapping surfaces can be dynamically advantageous for propulsion and flight under these conditions. Ramamurti and Sandberg [28] computed 2-D flow about pitching and heaving airfoils and compared their results with the experimental work of Anderson [29]. Although 2-D wing-section investigations can yield useful insights on the coupled pitching and heaving dynamics, it is essential to carry out 3-D computations to understand the influence of spanwise flow. We chose to pursue the fruit fly for computational investigations because both detailed wing kinematics and corresponding force data were available. Some of our computational results are summarized next.

Fruit Fly Wing

The configuration of the hovering *Drosophila melanogaster* is shown in Fig. 1. Computations are performed for various phase angles between the rotation and translation motions, and the time history of the unsteady forces is compared with the experimental results. The position of the wing is shown at three different times during the flapping cycle in Fig. 1b. The coordinate system (x', y', z') is fixed to the wing, and the wing rotates about the x axis (translation) and about the z' axis throughout the cycle. The kinematics of the wing motion are obtained from the experiments of Dickinson et al. [9]. The angle of rotation about the x axis (roll) and the z' axis (pitch) is shown in Fig. 2. Three different phases between the translational and rotational motions were used. In the advanced case, wing rotation precedes stroke reversal by 8% of the wing-beat cycle; symmetrical wing motion is when the wing rotation occurs symmetrically with respect to stroke reversal; and in delayed wing motion, rotation is delayed by 8% with respect to stroke reversal.

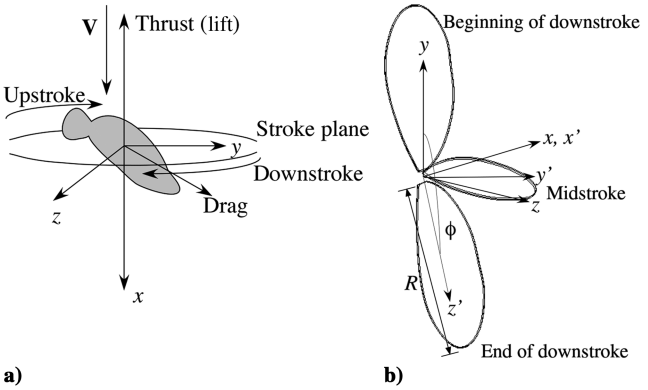

Fig. 1 Schematic of the a) flapping *Drosophila* wing and b) computational coordinate system.

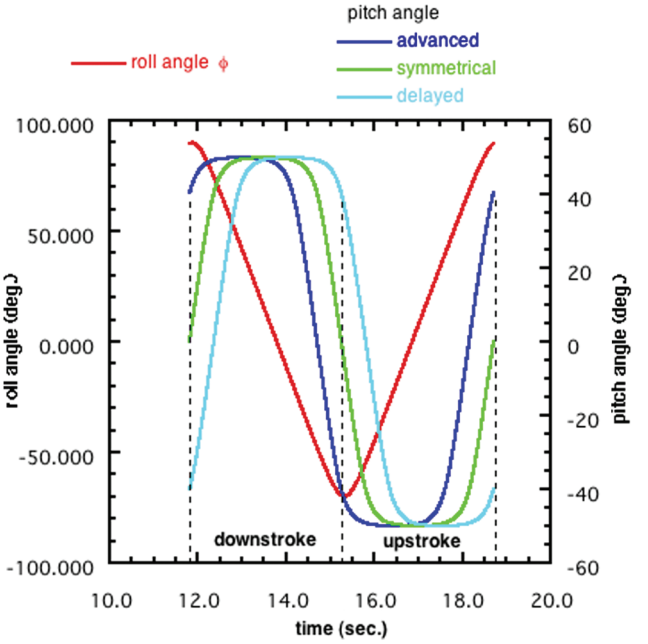

Fig. 2 Kinematics of the flapping *Drosophila* wing.

Wing-beat amplitude is 160 deg, flapping frequency is 0.145 Hz, and the angle of attack at midstroke is approximately 40 deg during both upstroke and downstroke.

The unsteady computation was carried out for five cycles of oscillation. Figures 3a and 3b show the comparison of thrust and drag forces, respectively, during one cycle of the wing beat. The comparison is good in that the present computations capture the peak forces well. We observe that the rotational mechanism is important and the combined translational and rotational mechanisms are necessary to accurately describe the force time histories and unsteady aerodynamics of flapping wings. In addition, we observe a wake-capture mechanism, proposed by Dickinson et al. [9], leading to lift enhancement at the beginning of stroke reversals. A possible explanation for the increase in thrust between t_1 and t_2 is that the wing moving through this wake benefits from the shed vorticity. A leading-edge vortex is created at the end of the preceding upstroke. This vortex is located below the wing and is rotating in the counterclockwise direction. As the wing moves through this vortex during the downstroke, it produces a stagnation region at the bottom of the wing, resulting in an increase in thrust. This effect is dependent on the kinematics of the wing near-stroke reversals and the freestream flow conditions. Also, we observe that when the wing rotation is advanced with respect to the stroke reversal, the peak in the thrust forces is higher than when the wing rotation is in phase with the stroke reversal, and the peak thrust is reduced further when the wing rotation is delayed.

Ellington [10] proposed the presence of stable helical leading-edge vortices throughout the stroke as a mechanism of producing high lift forces in insects. The structure of the leading-edge vortex is very difficult to observe throughout the stroke, and an instantaneous particle trace near midstroke (Fig. 4) shows the leading-edge vortex connected to the wing-tip vortex.

Effect of Gust Velocity

For vehicles with very small inertia, as in the case of MAVs, changes in wing loading can immediately affect the flight path. The need for suppressing the effects of wind gusts becomes important, more so when the airspeed of the vehicle decreases, because wind gusts become a large percentage of the mean airspeed of the vehicle. To study this, the downward gust velocity (Fig. 1a) is increased from a hovering condition to the mean wing-tip velocity (20 cm/s) and the unsteady computations are performed. The computed forces were nondimensionalized as follows:

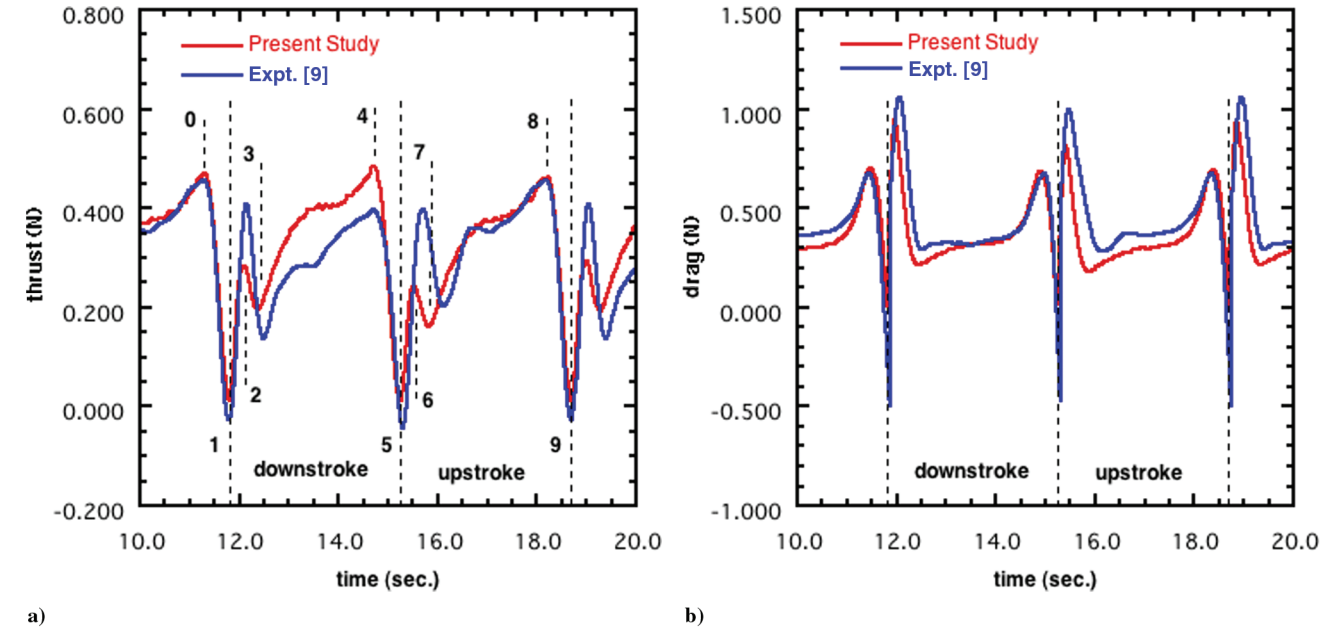

Fig. 3 Comparison of the time histories of a) thrust and b) drag forces.

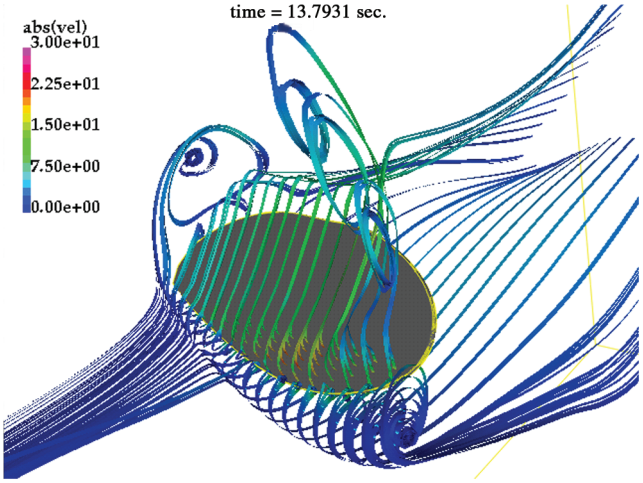

Fig. 4 Instantaneous particle traces during the middle of the downstroke, $t = 13.79$ s.

$$C_T = \frac{T}{\frac{1}{2}\rho U_t^2 \bar{c} R r_2^2(s)} \quad \text{and} \quad C_D = \frac{D}{\frac{1}{2}\rho U_t^2 \bar{c} R r_2^2(s)} \tag{3}$$

where ρ is the density of the mineral oil (880 kg m^{-3}), U_t is the mean wing-tip velocity, $r_2^2(s)$ is the second moment of the area (0.4), $\bar{c} = 2R/\mathrm{AR}$, and AR is the aspect ratio of the wing.

Figure 5 shows the time history of the thrust and drag forces during one cycle of the wing beat for the various gust velocities considered. The coefficient of thrust C_T achieves a maximum just before the stroke reversal (Fig. 5a). For a hovering case, this peak value is 2.05, and as the downward velocity is increased, the magnitude of this peak diminishes to 1.15 for the maximum downward velocity ($\boldsymbol{V} = 20$ cm s^{-1}) considered. The mean coefficient of thrust per cycle for the case is 1.307 and is reduced to -1.557 as $\boldsymbol{V}$ in increased to 20 cm s^{-1}. This effect is significant and one has to consider it for the development of a controller for a flapping-wing vehicle that is to be operational in a realistic scenario.

This effect is expected, because this peak is mainly due to the rotational effect of the wing, which is rotating in a counterclockwise direction about the y axis at the beginning of the downstroke. A downward velocity in the x direction will diminish the rotational effect that produces the lift, and hence the peak thrust is reduced. This rotational effect is also responsible for the increase in drag coefficient before stroke reversal seen in Fig. 5b. These rotation effect peaks also shift closer to the stroke reversal as the velocity is increased. From Fig. 5a, it is clear that a peak thrust is produced just after the stroke reversal. This peak is attributed to the wake-capture effect, in which the wing passes through the shed vorticity of the previous stroke. Figure 6 shows the velocity vectors on a $y = 10$-cm plane at the beginning of the downstroke. For symmetric rotation, the wing chord is aligned with the x axis at the beginning of the stroke reversal. For the hovering case, a vortex is seen near the leading edge on the bottom surface of the wing. This vortex was shed during the previous upstroke. As the downward gust velocity is increased, the strength of this vortex reduces in strength and disappears entirely at a velocity $\boldsymbol{V} = 20$ cm s^{-1}. This is due to the fact that the effective angle of attack α of the wing with respect to the combined velocity vector of the translational and downward velocity is reduced as the gust velocity is increased. The position of the wing at the end of the upstroke and beginning of the downstroke are shown in Fig. 7. Figure 8 shows the vorticity contours in the spanwise direction on a $z' = 10$-cm plane from the center of rotation. It is clear from Fig. 8a that the leading-edge vortex is formed during the upstroke in the hovering case. Before stroke reversal (Figs. 8a and 8b), a leading-edge vortex is seen on the bottom surface of the wing and continues to be present at stroke reversal (Fig. 8c) and beyond (Fig. 8d). At $t = 12.24$ s, this leading vortex from the previous upstroke disappears completely (Fig. 8e) and a vortex on the upper side of the wing begins to form (Fig. 8f).

Maneuvering Fruit Fly

The question of force production during insect turning has been addressed recently. Fry et al. [18] studied the wing and body kinematics of free-flying *Drosophila* performing rapid maneuvers, called *saccades*. They measured insect wing and body kinematics and used the data to drive a robotic model of the fruit fly. They measured the total aerodynamic force and torque during the specified saccade maneuver of the fly model. The results of the Fry et al. work indicated that inertia, rather than viscous effects, dominated the torque production. The details of the unsteady aerodynamics of force and yaw moment production by each of the two asymmetrically flapping wings interacting with the fly body, and how those were related to the overall insect torque production was still an open question. We investigated this question computationally, Ramamurti and Sandberg [17], and showed that subtle changes can result in the yaw moment required to perform the turning maneuver. The computed time history of force is compared (Fig. 9) with the

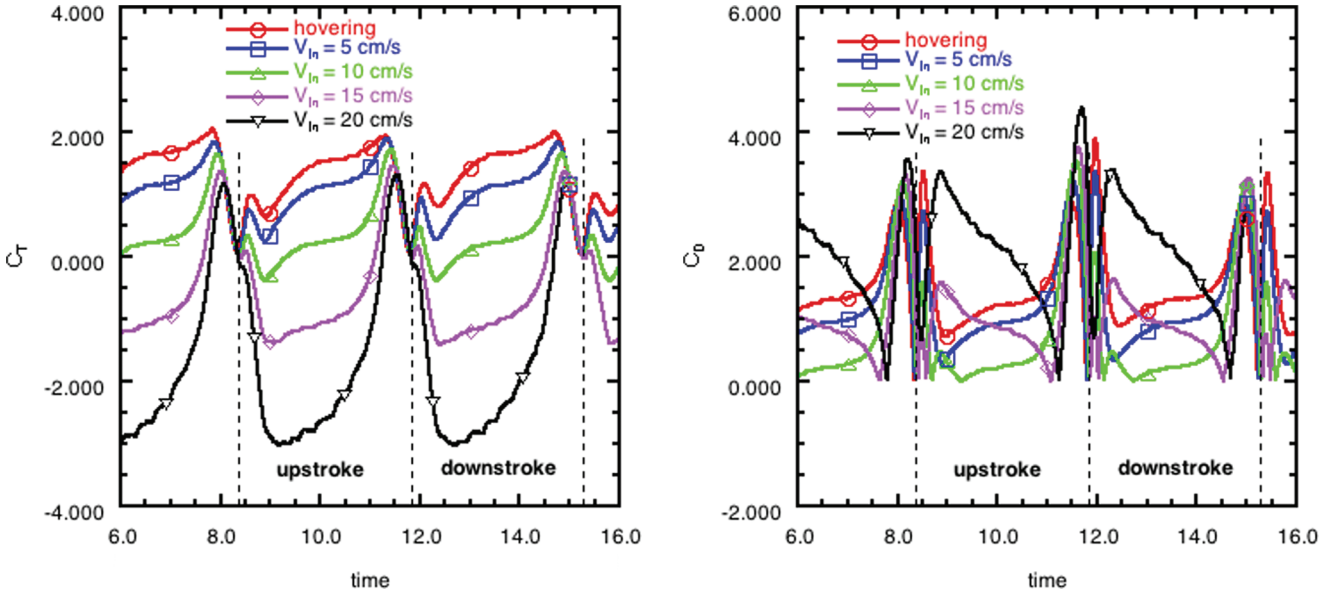

Fig. 5 Time variation of a) the thrust coefficient, b) drag coefficient through one cycle of flapping.

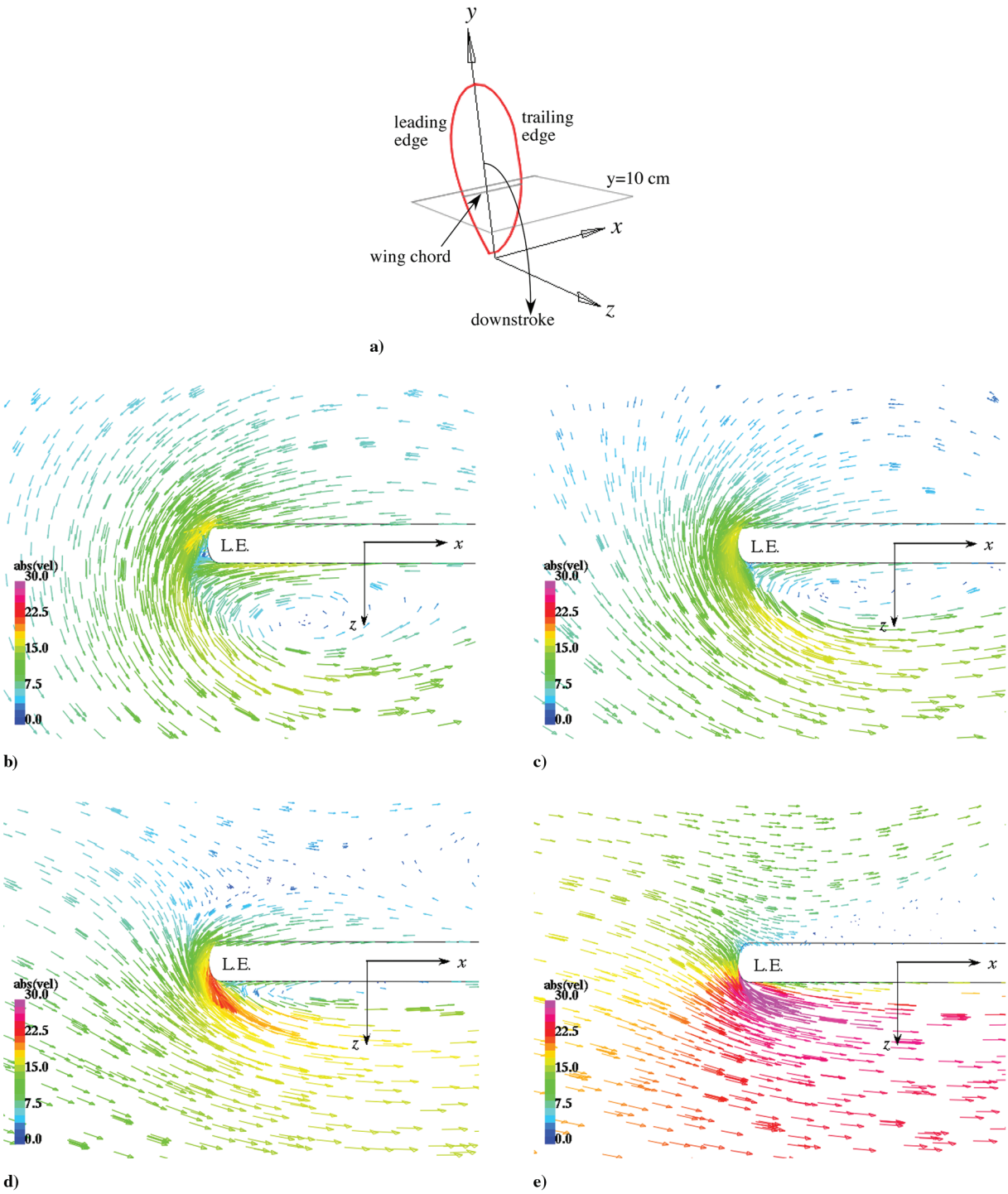

Fig. 6 Velocity vectors on $y = 10$-cm plane showing the effect of downward gust velocity on the leading-edge vortex at $t = 11.81$ s: a) position of the wing at the beginning of the downstroke, b) a large vortex shed from the previous upstroke is seen near the leading edge (L.E.) in hovering, c) and is smaller for $V_{in} = 5$ cm s^{-1}, d) reduces further in size for $V_{in} = 10$ cm s^{-1} and e) is absent for $V_{in} = 20$ cm s^{-1}.

measured values and is in excellent agreement throughout the entire *saccade* maneuver. Figure 10 shows the evolution of vorticity shed from the wings through one cycle in the middle of the *saccade* maneuver. The vortex loops shed from the leading edge and wing tip clearly show asymmetry between the right and left wings. The loop ahead of the body on the right wing is still connected at $t = 0.05328$ s, whereas on the left side, it has already pinched off. We can see the vortex shedding off of the leading edge at stroke reversal and being made into a loop through the downstroke. Between $t = 0.55$–0.57 s, we can see the Λ-like structure generated from the previous upstroke. This structure, in contrast to the hover cycle, exhibits asymmetry in the lengths of the legs mainly due to the leg on the left side formed due to pinching off at an earlier instant than that with the right side. A detailed description of the maneuvering results is given in Ramamurti and Sandberg [17]. These computations can be of value not only to biomimetic vehicle designers, but also to the biological community, because knowledge of surface-pressure-distribution time histories during insect, bird, or fish locomotion and maneuvering is essential to understanding the bone, muscle, and skin external loading experienced by these creatures as they execute such motions.

Swimming Fish

In addition to hovering and maneuvering insects, we are also interested in developing UUVs propelled by flapping wings. For our

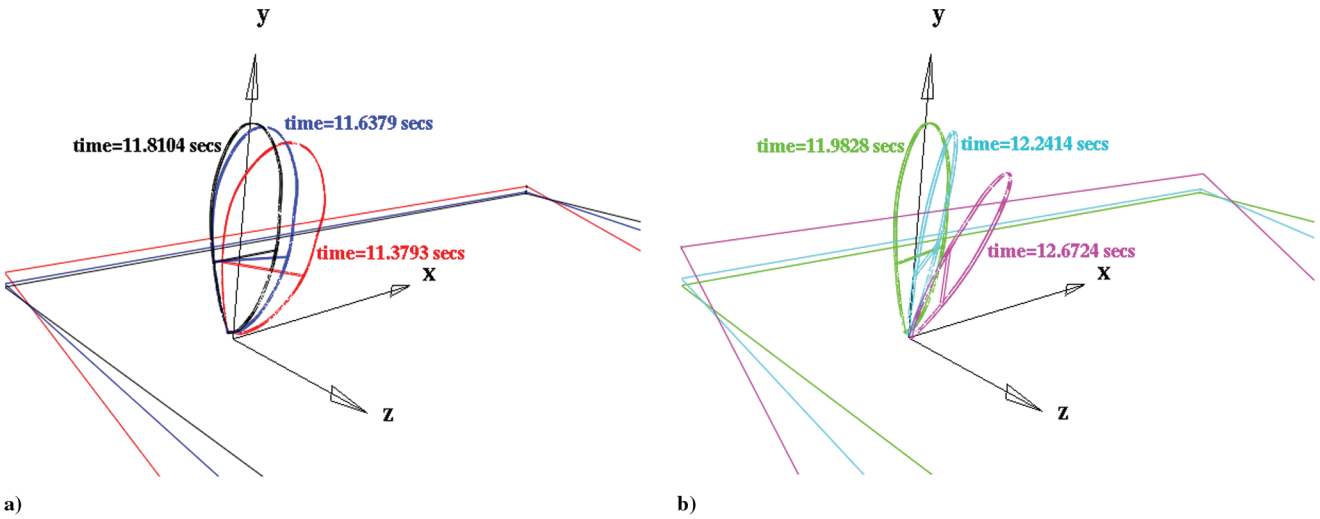

Fig. 7 Orientation of the wing at a) the end of the upstroke and b) the beginning of the downstroke. The $z' = 10$-cm plane for which the vorticity contours are shown is indicated.

next computation, we chose a flapping fin of a fish for which such data did exist. A candidate for which both fin kinematic data and corresponding fish accelerations were available [19] was the bird wrasse (*Gomphosus varius*). The bird wrasse had also been reported to have excellent low-speed maneuverability and good high-speed propulsion capabilities, characteristics that we desire in a vehicle. The 3-D surface coordinates of the bird wrasse, *G. varius*, and the kinematics of the flapping pectoral fin were obtained from Walker and Westneat [19]. In that work, the computations were performed using 14 control points to describe the motion of the deforming fin. The motions of these control points were obtained from three distal markers and smoothed using a quintic spline function. The three-dimensional unsteady computations of Ramamurti et al. [20] about the deforming pectoral fins using the experimentally measured fin kinematics were found to be in excellent agreement both in the time history of force production throughout the flapping strokes and in the magnitudes of the generated forces.

Effect of Rigidity of the Fin

A question that often arises is how important the flexibility of the fin is for force production and whether the deformation is active or passive. To address the first question, we carried out a set of unsteady computations for several cycles of the fin oscillation for fins of varying rigidity. The rigidity of the fin is varied by selecting a reduced number of control points. Figure 11 shows the control points along the fin tip at the instant when the fin is fully spread out from the body. All of the 14 control points that were supplied from experimental observation are shown in Fig. 11a. We can construct a fin that is rigid by using only one control point at the leading edge of the fin tip and the intersection of the leading- and trailing-edge rays with the body of the wrasse, as shown in Fig. 11b. The kinematics of this rigid fin follow from the motion of this single control point obtained from the experiments. Using the coordinates of this control point at various instants through the flapping cycle and the location of the root points at the leading and trailing edges, we can obtain the coordinates of the points on the fin tip, so that they lie on a plane. Next, the trailing-edge point was added to the list of control points, as shown in Fig. 11c, and another point was added at midchord along the fin tip. The resulting initial shape is shown in Fig. 11d. Finally, four control points were chosen out of the original 14, such that the leading-edge curvature of the fin is defined properly. The points that were chosen are the leading edge and two successive points close to the leading-edge and the trailing-edge points. The resulting shape is shown in Fig. 11e.

Unsteady simulations were carried out with the bird wrasse swimming at 45 cm/s so that we could compare the force production of the reduced flexibility cases with earlier computations for the fully deformable fin. The stroke amplitude is approximately 2.14 rad and the frequency of fin oscillation is 3.3 Hz for all configurations, resulting in a mean tip speed of approximately 50 cm/s. Computations were carried out for more than four cycles of fin oscillation using a computational mesh consisting of approximately 150,000 points and 840,000 tetrahedral elements for the four modified fin shapes. The time-varying 3-D lift and thrust, computed by integrating the surface pressure over the wrasse body and fin at each time step throughout the simulation, are shown in Fig. 12.

In the case of the rigid fin, a thrust with a peak value of 0.007 N is produced at the beginning of the downstroke, as shown in Fig. 12a. This is similar to the increase lift just after stroke reversal in the hovering *Drosophila*, reported by Dickinson et al. [9] and Ramamurti and Sandberg [16] and is attributed to the wake-capture mechanism. The thrust then quickly drops and a drag force is produced for the remainder of the downstroke. In the case of the flexible fin with two control points (namely, the leading and trailing edges of the fin tip), the wake-capture peak is absent and no positive thrust is produced during the entire downstroke. In contrast, all the other cases of the partially flexible fins produce the same thrust during the downstroke as the fully deformable fin with motion prescribed by all 14 control points, starting near zero at the beginning of the downstroke and increasing to a maximum of 0.008 N at about 30% of the downstroke. During the upstroke, the rigid fin produces a peak thrust of 0.022 N at about 61% of the upstroke, compared with a peak value of 0.046 N produced by the flexible fin at 64% of the upstroke. The flexible fin with two control points achieves a peak value of 0.046 N, but at an earlier time, at about 47% of the upstroke.

The thrust produced in the case of the flexible fin with three control points is very similar to the fully flexible case. If only the leading-edge curvature of the fin is retained, as in the case with four control points, the peak thrust achieved during the upstroke is 0.0675 N and occurs at approximately 60 and 92% of the upstroke. It is clear that the results using three control points matched exactly with the results obtained using all 14 control points. This is to be expected, because the motions of the 14 control points in the experiments were derived from these three points, except for the fact that the shape of the wing tip of the fin is defined by a parabola for the three-point case instead of by a piecewise cubic spline as for the 14-control-point case. During the downstroke, the lift (shown in Fig. 12b) produced by the flexible fin using 3, 4, and 14 control points attains a peak value of approximately 0.08 N at 37% of the downstroke; a peak lift of 0.123 N is attained at 30% of downstroke with the leading- and trailing-edge control points; and a maximum lift of 0.16 N is attained at about 40% of the downstroke with a fully rigid fin. But the rigid fin loses the lift during the upstroke, with a minimum lift of −0.37 N at about 50% of the upstroke. The minimum lift attained in the case with two control points is approximately −0.145 N, which occurs at

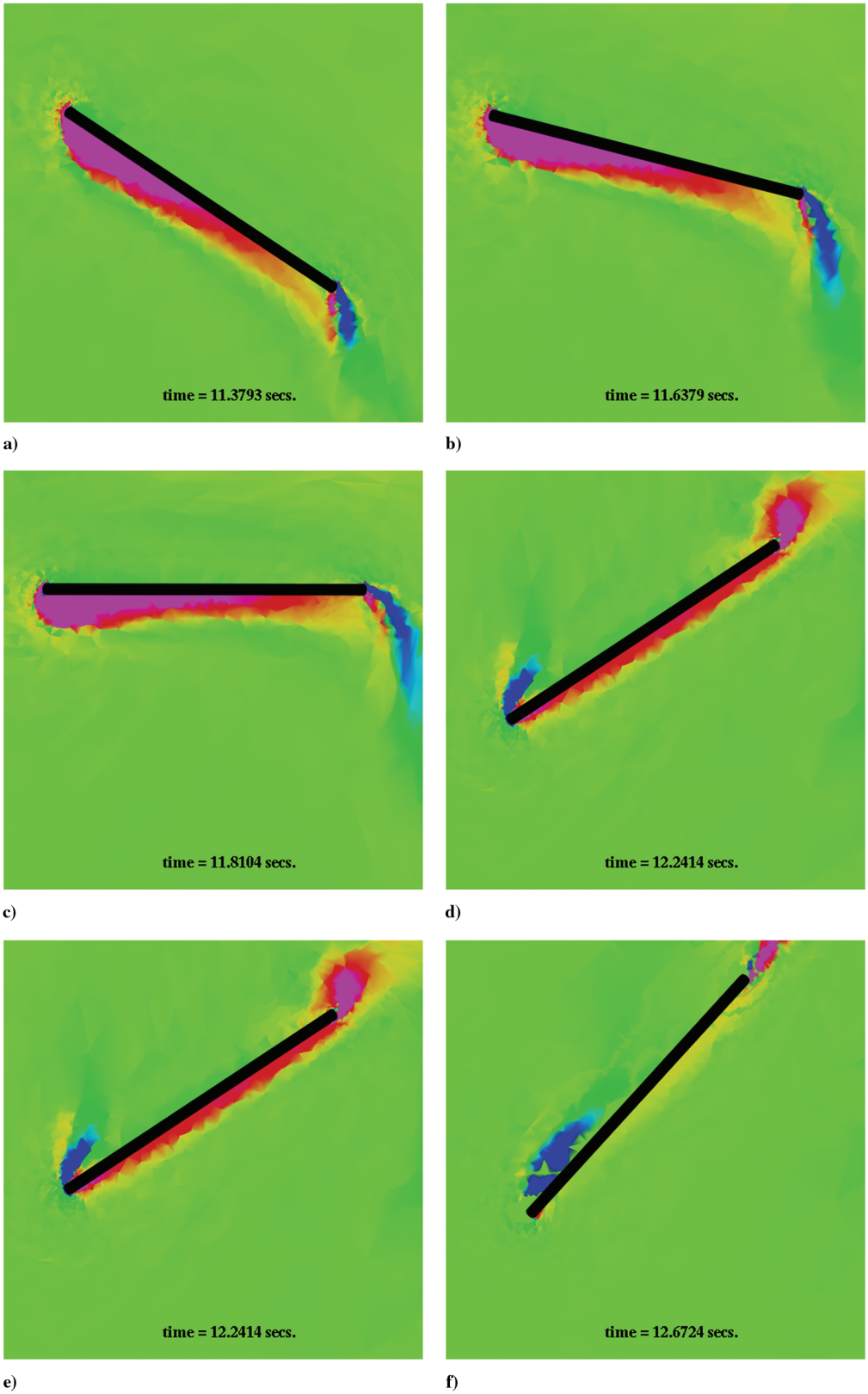

Fig. 8 Vorticity contours on the $z' = 10$-cm plane during stroke reversal.

about 39% of the upstroke, and for the case with four control points, a minimum lift of −0.104 N is attained at about 43% of the upstroke. Again, the case with three control points matches exactly with the fully flexible fin, as expected. These results suggest that the fish or a vehicle with a rigid fin or the fin controlled by just two points will experience much larger-amplitude vertical excursions than with a flexible fin.

Application to Unmanned Vehicles

Although many flapping-wing vehicles, such as ornithopters, tend to directly mimic the flight and control of birds or insects, it is possible to use flapping-foil principles in ways that are inspired by biological flight mechanisms but do not copy them directly: so-called biomorphic flying configurations. For example, "aerial swimming" vehicles can use a single reversing-camber flapping

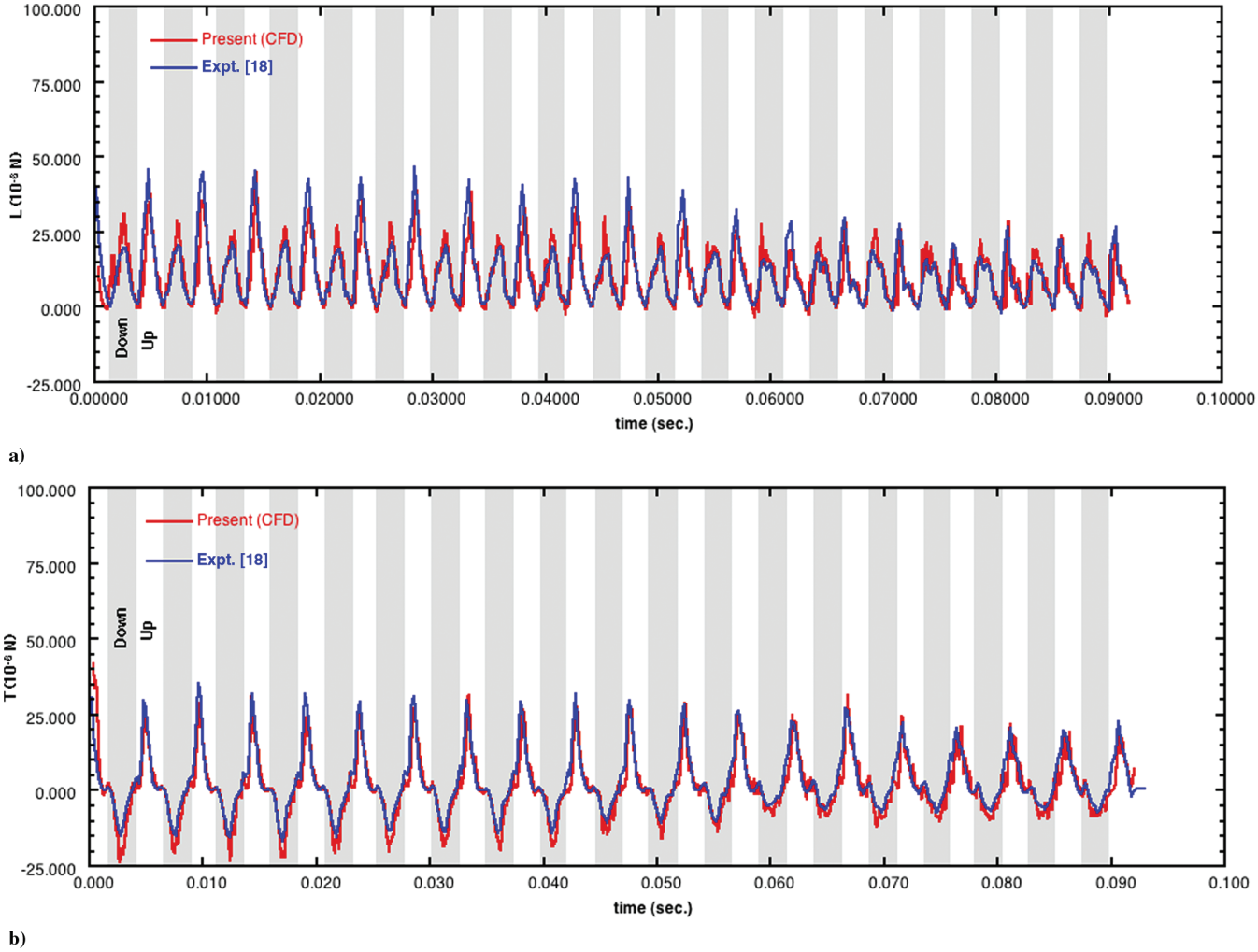

Fig. 9 Comparison of the time histories of a) lift and b) thrust forces.

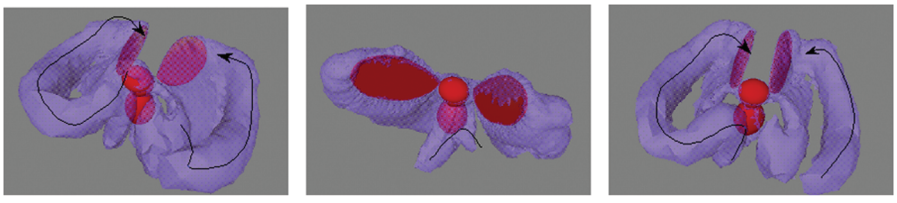

t = 0.05328 s t = 0.05614 s t = 0.05834 s

Fig. 10 Contours of isovorticity shed by the fruit fly during *saccade* maneuver.

wing at the rear, in contrast to a set of normal biological wings. Two other biomorphic configurations to be treated in some detail later are the clapping reversing-camber airfoil, which creates and makes use of pressure pulses to augment thrust, and the tandem pair of clapping reversing-camber airfoils, which provide both thrust and lift.

Our initial flapping-airfoil configurations were hybrid fixed/flapping-wing vehicles, in that they each had fixed-wing surfaces that provided most of the lift necessary for sustained flight. Birds and insects, in general, do not have substantial fixed lifting surfaces unrelated to propulsion and control. To more closely approach this biological feature and its potential advantages, another configuration was developed that has no fixed lifting surfaces and uses two tandem sets of clapping pairs of reversing-camber wings for both thrust and lift. The biplane insectoid travel engine (BITE wing) shown in Fig. 13 employs several mechanisms common to insect locomotion for both flight and ground mobility. We have carried out computational investigations to achieve a better understanding of the action of the reversing-camber foils, the effects of the clapping interaction, and the interaction between the front and rear pairs of wings. In particular, we carried out numerous unsteady simulations investigating the interactions between the wings of each pair, as well as the interactions between the two pairs. Some results from these simulations are shown in Fig. 14. The MAV vehicle design investigations are described by Kellogg et al. [30] and Ramamurti et al. [31]. The force time history from the simulation using prescribed kinematics is shown in Fig. 15. The thrust reaches a peak of 0.004 lb during the downstroke and a value of 0.0158 lb during the upstroke, with a net drag of 0.0056 lb during the cycle. Also, most of the total thrust is produced by the rear pair of wings, and the contribution from the front pair is a net drag. The lift reaches a peak value of 0.057 lb at 0.253 s during the downstroke and reaches 0.05 lb

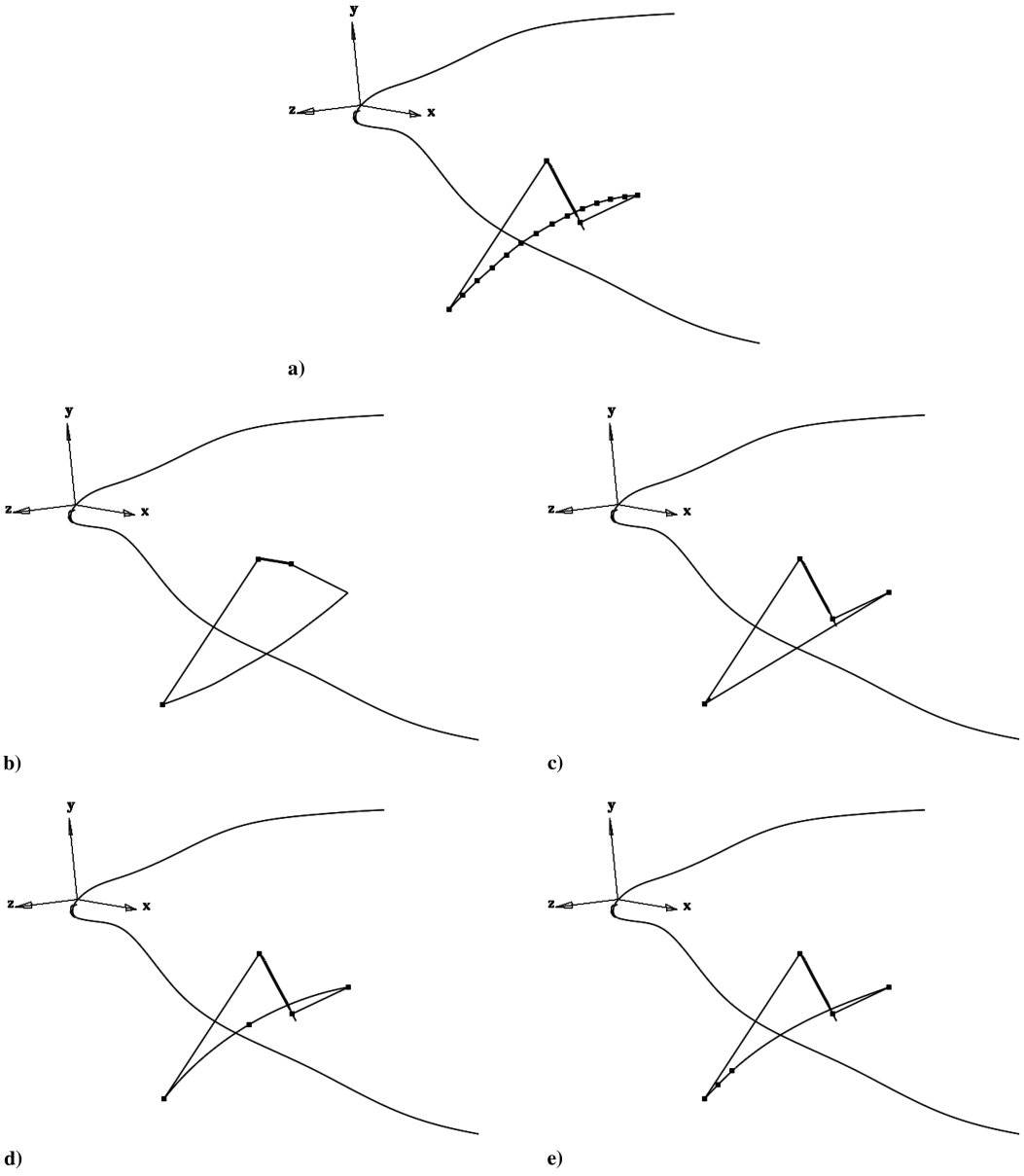

Fig. 11 Shapes of the fully deformable bird wrasse fin and modified fin at an instant when the fin is fully extended: a) experimentally observed deformable fin with 14 control points, b) modified rigid fin with a control point on the leading edge and at the tip of the fin, c) flexible fin with control points at the leading and trailing edges of the fin tip, d) flexible fin with three control points, and e) flexible fin with four control points closer to the leading edge.

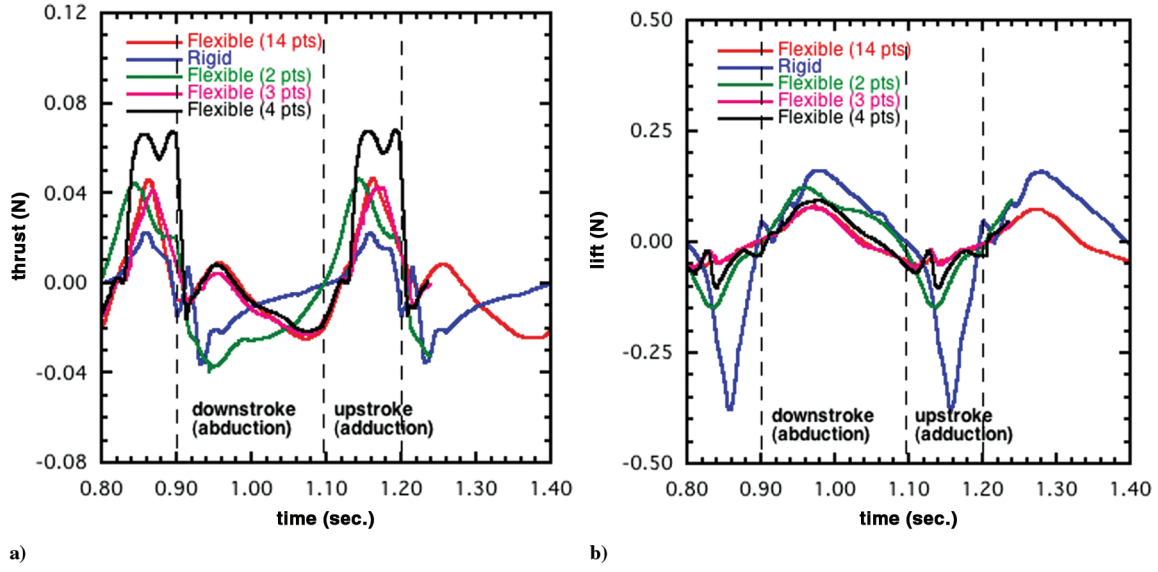

Fig. 12 Effect of fin flexibility on the time variation of a) thrust and b) lift forces.

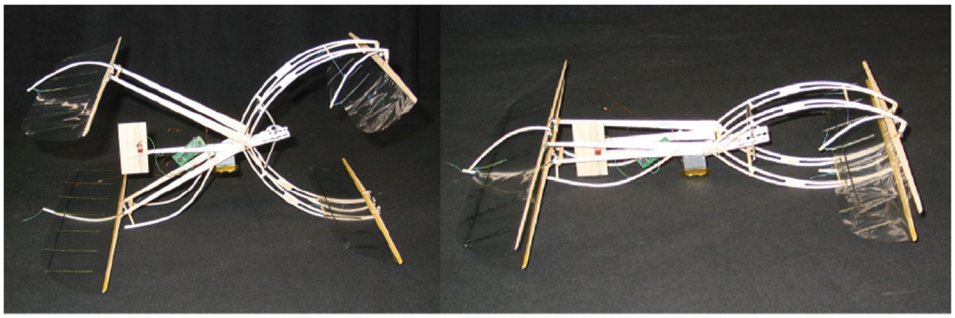

Fig. 13 A radio-controlled BITE-wing vehicle with foils separated shown in the left view and in the clapping position shown in the right view.

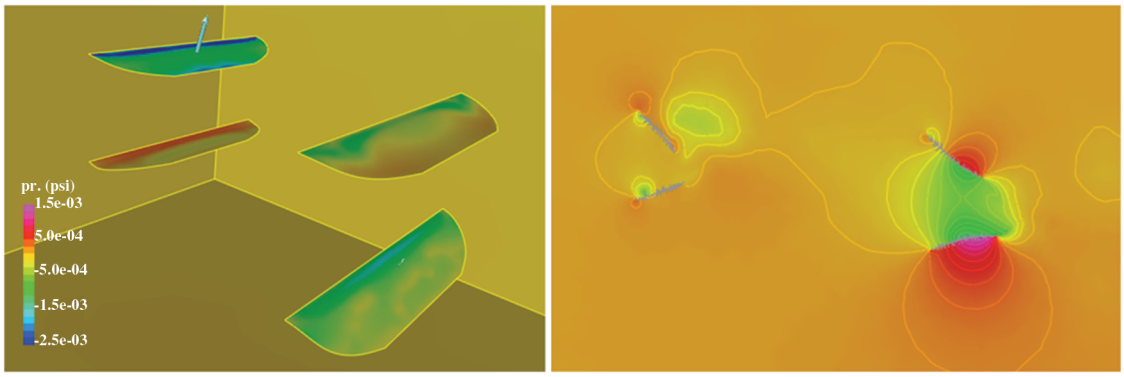

a) b)

Fig. 14 Flow past the four flapping wings of the BITE vehicle: a) instantaneous pressure distribution and b) instantaneous vorticity field.

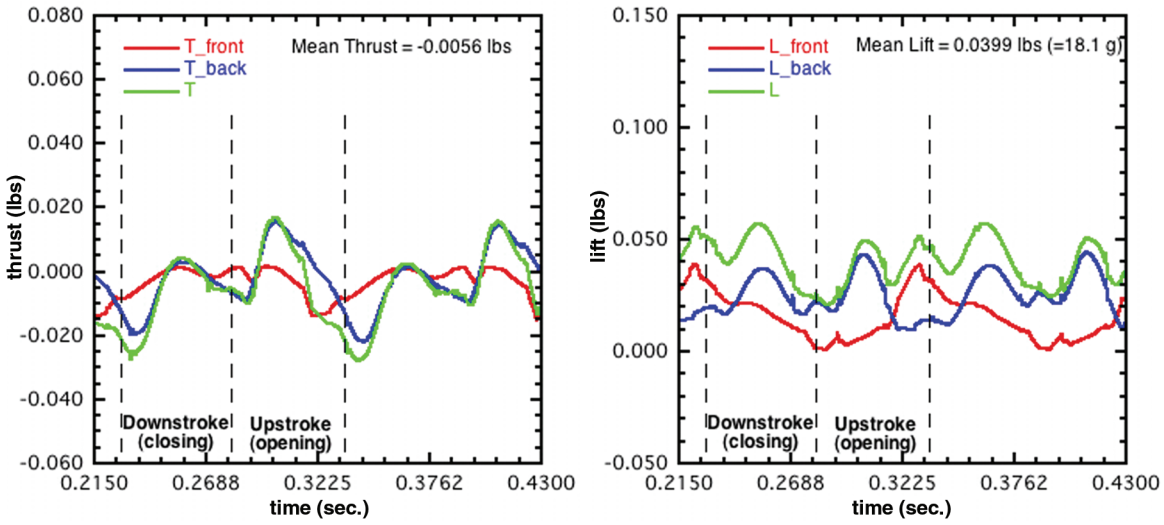

a) b)

Fig. 15 Thrust and lift production of the BITE wing with smoothed kinematics.

at two instants, 0.3 and 0.33 s, during the upstroke. These peaks correspond to the portion of the stroke in which the wing membrane has completed its camber reversal and its cross-sectional shape has reached an equilibrium point. Increasing the plunge distance of the wing should lengthen the time that these conditions apply to the wing, thus lengthening the midstroke peaks of lift and thrust. Effectively, a longer plunge increases the portion of the cycle time that the wings are producing thrust, and a smaller chord reduces the time that the wings spend reversing camber. The result is analogous to the increased efficiency of lower disk loadings in a rotary wing; greater momentum transfer is achieved for the same energy expenditure by increasing the mass flow rather than the flow velocity.

Unmanned Underwater Vehicles

We designed an unmanned underwater vehicle for the purpose of demonstrating the propulsive performance of the NRL actively controlled curvature fins. The details of the controlled curvature fin design, the fin construction and testing, and the vehicle design are described by Palmisano et al. [32]. Our initial prototype

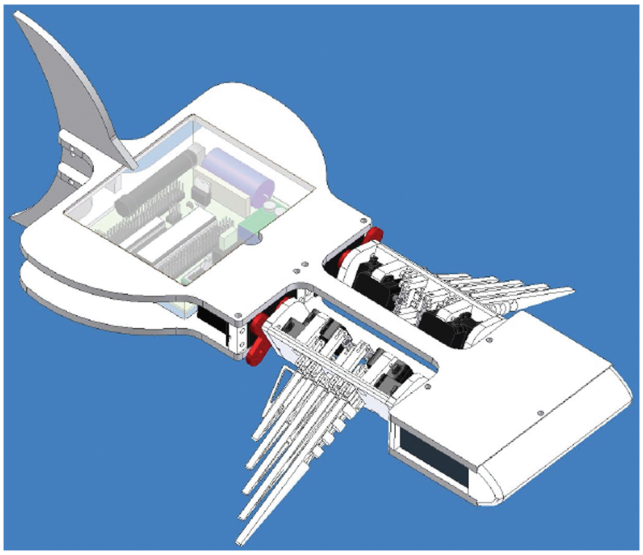

Fig. 16 Test vehicle for carrying a set of two NRL actively controlled curvature fins.

demonstration vehicle incorporates two fins that are an integration of individually designed compliant structural fin rays, individual linear actuation servos, and a polymeric membrane skin to produce the desired surface-curvature time histories, resulting in the production of propulsive-force time histories. The vehicle with its two fins is shown in Fig. 16.

Three-dimensional unsteady computations of a notional UUV with a flapping fin have been carried out. Several parameters in the design of the flapping fins were varied and described in detail by Ramamurti and Sandberg [33]. Based on our previous study on the effect of rigidity of the bird wrasse fin on the force production in fish, the number of ribs for the current flapping fin is reduced to five. This is done to reduce the complexity of the mechanical system. The important parameters that govern the thrust production are the angle of attack of the root section of the fin, the frequency, and the amplitude of flapping. After several parametric studies varying the angle of attack of the root section of the fin, it was found that 20i was near optimum. The original NRL kinematics was modified so that the amplitude of the oscillation is 114 deg and the frequency is 1 Hz. The time history of forces generated by the flapping fin is shown in Fig. 17. The thrust produced in this case has a mean value of −0.32 N and the mean lift is 0.58 N. The minimum and maximum values of

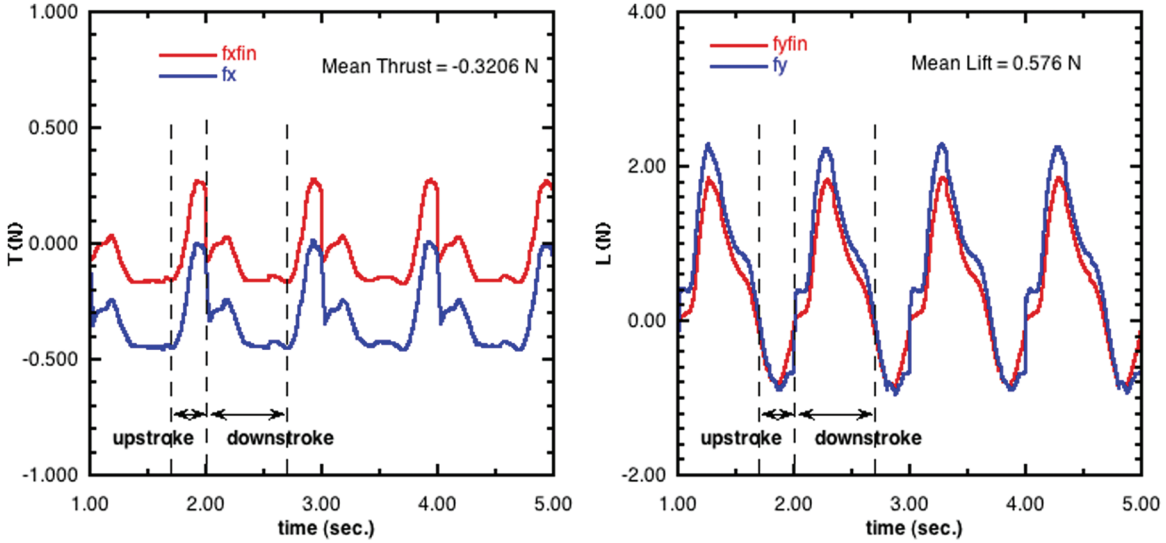

Fig. 17 Thrust and lift production for a UUV moving at 3 kt, $\alpha_r = 20\,\text{deg}$, $\phi_{\max} = 114\,\text{deg}$, $f = 1.0$ Hz.

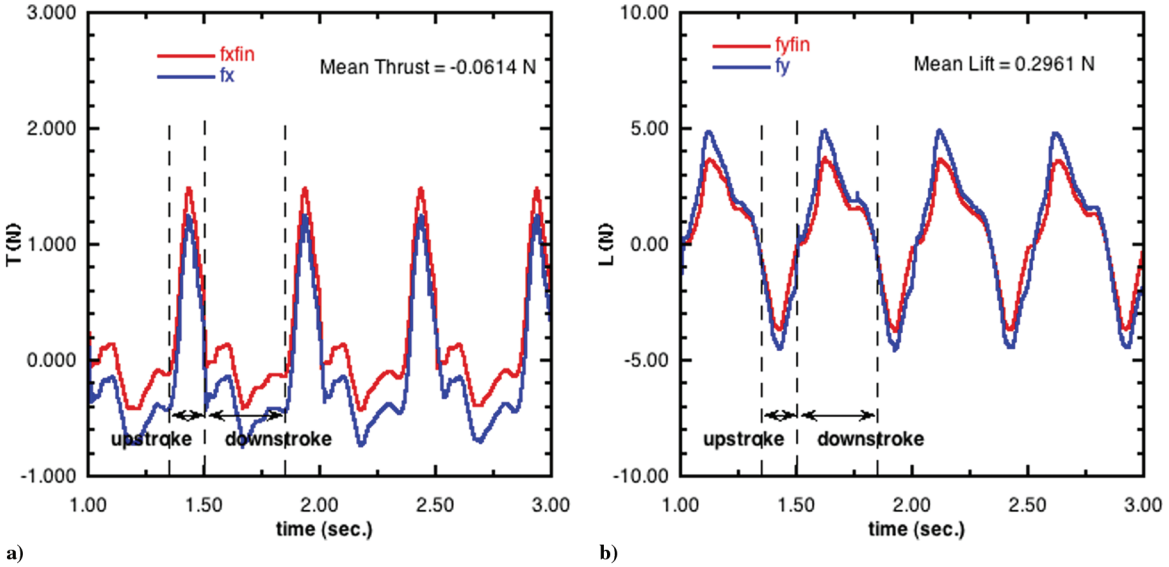

Fig. 18 Thrust and lift production for a UUV moving at 3 kt, $\alpha_r = 20\,\text{deg}$, $\phi_{\max} = 114\,\text{deg}$, $f = 2.0$ Hz.

the lift force during the cycle are −0.95 and 2.3 N, respectively. As the frequency of oscillation is increased from 1 to 2 Hz (Fig. 18), the mean thrust is nearly zero (−0.06 N). Because the inflow velocity in these computations is 3 kt, we are in equilibrium (or, in the absence of a current, the vehicle will move at 3 kt).

Conclusions

The aerodynamic characteristics of micro air vehicles, flapping propulsion in a hovering and maneuvering fruit fly, and the pectoral-fin swimming in fish were computationally investigated using a finite element flow solver based on unstructured, adaptively remeshed grids. Some of the mechanisms observed in nature were incorporated in constructing unconventional aerial and underwater vehicles. We also performed unsteady flow computations over the *Drosophila* wing with the flight conditions ranging from hovering to a downward gust velocity nearly equal to the mean wing-tip velocity. The effect of this downward velocity is a reduction in the rotational forces that produces a peak in the thrust and drag just before stroke reversal. We showed that the wake-capture mechanism that is responsible for a peak in thrust production just after stroke reversal diminished with increasing downward velocity and is entirely absent when this velocity reaches the mean wing-tip velocity. The unsteady computations of the swimming bird wrasse fish using the prescribed kinematics of the pectoral fin were performed for varying rigidity of the fin, ranging from a fully rigid to a fully deformable fin, by selecting a reduced number of control points used to define the fin kinematics. We found that when the fin is made rigid by specifying the motion with just the leading edge of the fin tip, the thrust produced during the upstroke is less than half of the peak thrust produced by the flexible cases. From the point of view of lift production, we found that all of the cases with flexible fins performed in a similar manner, except the fin controlled by just the leading- and trailing-edge points. In the case of the rigid fin, there was a substantial loss of lift during the upstroke. Therefore, a fish or a vehicle with rigid fin or a fin controlled by just the leading- and trailing-edge points would experience more vertical excursions than one with a flexible fin. A fully coupled simulation of the interaction of the fluid forces and the structural deformation of the flapping wing is needed to obtain further insight into the role of deformation on the force production in flapping wings.

Acknowledgments

This work was supported by the Office of Naval Research through the Tactical Electronic Warfare Division of the Naval Research Laboratory (NRL). This work was supported in part by a grant of High-Performance Computing (HPC) Center time from the U.S. Department of Defense HPC Centers, U.S. Army Research Laboratory, Major Shared Resource Centers SGI-O2K and NRL SGI-O2K. The authors would like to thank Rainald Löhner of George Mason University and J. Kellogg and B. Ratna of NRL for their helpful discussions and assistance throughout the course of this work.

References

[1] Cook, N., "USA's Revolutionary Plan for Air Vehicles Unveiled," *Jane's Defence Weekly*, Mar. 1997.

[2] Evers, S., "'Culture of Innovation' Return to UAV Projects," *Jane's Defence Weekly*, Mar. 1997, p. 14.

[3] Hewish, M., "Building a Bird's-Eye View of the Battlefield," *Jane's International Defense Review*, Feb. 1997, pp. 55–56.

[4] Canan, J. W., "Seeing More, and Risking Less, with UAVs," *Aerospace America*, Oct. 1999, pp. 27–29.

[5] Wilson, R., "Mini Technologies for Major Impact," *Aerospace America*, May 1998, pp. 36–42.

[6] Hewish, M., "Rucksack Reece Takes Wing," *Jane's International Defense Review*, Feb. 1997, p. 63.

[7] Shyy, W., Berg, M., and Ljungqvist, D., "Flapping and Flexible Wings for Biological and Micro Air Vehicles," *Progress in Aerospace Sciences*, Vol. 35, July 1999, pp. 455–506. doi:10.1016/S0376-0421(98)00016-5

[8] Shyy, W., Klevebring, F., Nilsson, M., Sloan, J., Carroll, B., and Fuentes, C., "Rigid and Flexible Low Reynolds Number Airfoils," *Journal of Aircraft*, Vol. 36, No. 3, 1999, pp. 523–529.

[9] Dickinson, M. H., Lehmann, F.-O., and Sane, S. P., "Wing Rotation and the Aerodynamic Basis of Insect Flight," *Science*, Vol. 284, June 1999, pp. 1954–1960. doi:10.1126/science.284.5422.1954

[10] Ellington, C. P., "The Aerodynamics of Hovering Insect Flight, IV, Aerodynamic Mechanisms," *Philosophical Transactions of the Royal Society of London, Series B: Biological Sciences*, Vol. 305, Feb. 1984, pp. 79–113. doi:10.1098/rstb.1984.0052

[11] Liu, H., and Kawachi, K., "A Numerical Study of Insect flight," *Journal of Computational Physics*, Vol. 146, No. 1, Oct. 1998, pp. 124–156. doi:10.1006/jcph.1998.6019

[12] Willmott, A. P., and Ellington, C. P., "The Mechanics of Flight in the Hawkmoth Manduca Sexta, 2: Aerodynamic Consequences of Kinematics and Morphological Variation," *Journal of Experimental Biology*, Vol. 200, Nov. 1997, pp. 2723–2745.

[13] Aono, H., and Liu, H., "A Numerical Study of Hovering Aerodynamics in Flapping Insect Flight," *Bio-mechanisms of Swimming and Flying*, edited by N. Kato and S. Kamimura, Springer, New York, 2007.

[14] Sun, M., and Tang, J., "Unsteady Aerodynamic Force Generation by a Model Fruitfly Wing in Flapping Motion," *Journal of Experimental Biology*, Vol. 205, No. 1, Jan. 2002, pp. 55–70.

[15] Sun, M., and Wu, J. H., "Aerodynamic Force Generation and Power Requirements in Forward Flight in a Fruit Fly with Modeled Wing Motion," *Journal of Experimental Biology*, Vol. 206, Sept. 2003, pp. 3065–3083. doi:10.1242/jeb.00517

[16] Ramamurti, R., and Sandberg, W. C., "A Three-Dimensional Computational Study of the Aerodynamic Mechanisms of Insect Flight," *Journal of Experimental Biology*, Vol. 205, No. 10, May 2002, pp. 1507–1518.

[17] Ramamurti, R., and Sandberg, W. C., "A Computational Investigation of the 3-D Unsteady Aerodynamics of Drosophila Hovering and Maneuvering," *Journal of Experimental Biology*, Vol. 210, No. 5, Mar. 2007, pp. 881–896. doi:10.1242/jeb.02704

[18] Fry, S. N., Sayaman, R., and Dickinson, M. H., "The Aerodynamics of Free-Flight Maneuvers in Drosophila," *Science*, Vol. 300, Apr. 2003, pp. 495–498. doi:10.1126/science.1081944

[19] Walker, J. A., and Westneat, M. W., "Labriform Propulsion in Fishes: Kinematics of Flapping Aquatic Flight in the Bird Wrasse, Gomphosus Varius (Labridae)," *Journal of Experimental Biology*, Vol. 200, No. 11, June 1997, pp. 1549–1569.

[20] Ramamurti, R., Sandberg, W. C., Löhner, R., Walker, J. A., and Westneat, M. W., "Fluid Dynamics of Flapping Aquatic Flight in the Bird Wrasse: 3-D Unsteady Computations with Fin Deformation," *Journal of Experimental Biology*, Vol. 205, Oct. 2002, pp. 2997–3008.

[21] Ramamurti, R., and Löhner, R., "Evaluation of an Incompressible Flow Solver Based on Simple Elements," *Advances in Finite Element Analysis in Fluid Dynamics*, Vol. 137, Fluids Engineering Div., American Society of Mechanical Engineers, New York, 1992, pp. 33–42.

[22] Ramamurti, R., Löhner, R., and Sandberg, W. C., "Evaluation of a Scalable 3-D Incompressible Finite Element Solver," AIAA Paper 94-0756, Washington, D.C., 1994.

[23] Ramamurti, R., Löhner, R., and Sandberg, W. C., "Simulation of a Torpedo Launch Using a 3-D Incompressible Finite Element Flow Solver," AIAA Paper 95-0086, Washington, D.C., 1995.

[24] Ramamurti, R., Löhner, R., and Sandberg, W. C., "Computation of the 3-D Unsteady Flow Past Deforming Geometries," *International Journal of Computational Fluid Dynamics*, Vol. 13, No. 1, 1999, pp. 83–99. doi:10.1080/10618569908940891

[25] Kellogg, J., Bovais, C., Dahlburg, J., Foch, R., Gardner, J., Gordon, D., Hartley, R., Kamgar-Parsi, B., McFarlane, H., Pipitone, F., Ramamurti, R., Sciambi, A., Spears, W., Srull, D., and Sullivan, C., "NRL MITE Vehicle," *Proceedings of the 16th International UAV Systems Conference*, Univ. of Bristol, Bristol, England, U.K., Apr. 2001.

[26] Ramamurti, R., and Sandberg, W. C., "Computations of the Aerodynamics of a Micro Air Vehicle," *Progress in Astronautics and Aeronautics*, edited by T. J. Mueller, Vol. 195, AIAA, Reston, VA, 2001, pp. 537–555.

[27] Kellogg, J., Bovais, C., Cylinder, D., Dahlburg, J., Foch, R., Platzer, M., Ramamurti, R., and Sandberg, W. C., "Non Conventional

Aerodynamics for Micro-UAVs," *Proceedings of the 16th International UAV Systems Conference*, Univ. of Bristol, Bristol, England, U.K., Apr. 2001.

[28] Ramamurti, R., and Sandberg, W. C., "Simulation of Flow About Flapping Airfoils Using a Finite Element Incompressible Flow Solver," *AIAA Journal*, Vol. 39, No. 2, 2001, pp. 253–260.

[29] Anderson, J. M., "Vorticity Control for Efficient Propulsion," Ph. D. Dissertation, Massachusetts Inst. of Technology, Cambridge, MA, Feb. 1996.

[30] Kellogg, J., Bovais, C., Foch, R., Cylinder, D., Ramamurti, R., Sandberg, W. C., Gardner, J., Srull, D., Piper, G., and Vaiana, P., "Development and Testing of Unconventional Micro Air Vehicle Configurations," AIAA Paper 2003-6356, 2003.

[31] Ramamurti, R., Sandberg, W. C., Vaiana, P., Kellogg, J., and Cylinder, D., "Computational Fluid Dynamics of Unconventional Air Vehicle Configurations," *The Aeronautical Journal*, Vol. 109, No. 1097, July 2005, pp. 337–347.

[32] Palmisano, J., Ramamurti, R., Lu, K., Cohen, J., Sandberg, W. C., and Ratna, B., "Design of a Biomimetic Controlled-Curvature Robotic Pectoral Fin," *IEEE International Conference on Robotics and Automation*, Inst. of Electrical and Electronics Engineers, Piscataway, NJ, Apr. 2007, pp. 966–973.

[33] Ramamurti, R., and Sandberg, W. C., "Computational Fluid Dynamics Study for Optimization of a Fin Design," AIAA Paper 2006-3658, 2006.

G. Abate
Guest Editor